Journal of Structural Biology 163 (2008) 61–75

Contents lists available at ScienceDirect

Journal of Structural Biology

journal homepage: www.elsevier.com/locate/yjsbi

Macromolecular structure of the organic framework of nacre in *Haliotis rufescens*: Implications for growth and mechanical behavior

Jiddu Bezares [a], Robert J. Asaro [a,*], Marilyn Hawley [b]

[a] *Department of Structural Engineering, University of California, San Diego, Mail Code 0085, La Jolla, CA 92093, USA*
[b] *Materials Science and Technology Division, Los Alamos National laboratory, Los Alamos, NM 87545, USA*

ARTICLE INFO

Article history:
Received 8 January 2008
Received in revised form 8 April 2008
Accepted 9 April 2008
Available online 25 April 2008

Keywords:
Mollusk nacre
Biomineralization
Mollusk organic framework

ABSTRACT

We have performed a macromolecular structural analysis of the interlamellar and intertabular parts of the organic framework of the nacreous part of the shell of *Haliotis rufescens*, including the identification of structural chitin. Using histochemical optical microscopy we have mapped the locations of carboxylates and sulfates of proteins and chitin on the surfaces and within the core of the interlamellar layers and the intertabular matrix that together form the external organic matrix of composite nacre. This extends the earlier work of Nudelmann et al. [Nudelman, F., Gotliv, B.A., Addadi, L. and Weiner, S. 2006. Mollusk shell formation: mapping the distribution of organic matrix components underlying a single aragonite tablet in nacre. J. Struct. Biol. 153, 176–187] and Crenshaw and Ristedt [Crenshaw, M.A., Ristedt, H. 1976. The histochemical localization of reactive groups in septal nacre from *Nautilus pompilius*. In: Omori, M., Watabe, N. (Eds.) The Mechanisms of Biomineralization in Animals and Plants. Tokai University Press, Toyko] on *Nautilus pompilius*. Our mapping identifies distinct regions, defined by the macromolecular groups, including what is proposed to be the sites of $CaCO_3$ nucleation and that play a key role in nacre growth. Using AFM scanning probe microscopy we have identified a fibrous core within the framework that we associate with chitin. The structural picture that is evolved is then used to develop a simple structural model for the organic framework which is shown to be consistent with mechanical property measurements. The role of the intracrystalline matrix within the nacre tablets in mediating nacre's mechanical response is noted within the framework of our model.

1. Introduction

Biomineralization is a well regulated process within living organisms, and involves control over, *inter alia*, the morphology of mineral-biopolymer nano-composite structures, crystal nucleation within, and growth of, such structures, along with their polymorph type(s) and crystallographic texture (*e.g.* Lowenstam and Weiner, 1989; Simkiss and Wilbur, 1989; Mann et al., 1989; Baeuerlein, 2000; Addadi and Weiner, 2001). In mollusk shells, among a wide array of other cases, mineralization appears to occur within a preformed 3-dimensional organic framework which acts as the template that provides the above mentioned control (*e.g.* Bevelander and Nakahara, 1969; Wada, 1972; Schaffer et al., 1997; Nudelman et al., 2006). The organic framework thus mediates the growth, *i.e.* the "fabrication", of the mineralized nano-composite and, as it happens, is also key to what is seen to be a rather excellent array of mechanical properties of the shell (*e.g.* Sarikaya et al., 1992; Evans et al., 2001). It is, accordingly, vital to understand the structure of the organic framework and in particular its macromolecular layout so that critical features such as the crystal nucleation site(s) and the chemical/structural morphology that control mechanical behavior may be understood in a more quantified manner. Possible extensions of such understanding include biomimetic applications to, for example, nano-scale ceramic/polymer electronic devices and synthetic bone implants.

Crenshaw and Ristedt (1976) took a unique approach to studying the macromolecular structure in that they attempted a mapping of the framework's components using histochemical light microscopy. This approach has been recently pursued by Nudelman et al. (2006) who identify four different zones on the framework surface. This information was then shown to be of immediate use for formulating more detailed and defensible models for the biomineralization process. Crenshaw and Ristedt's (1976) and Nudelman et al.'s (2006) work was performed on the cephalopod *Nautilus pompilius*, whereas the latter performed comparative study on the bivalve *Atrina rigida*. Here, we again extend the approach, but for the case of the gastropod *Haliotis rufescens*, with comparative study on *N. pompilius* so as to obtain a more comprehensive understanding of the commonality and variances among different members of the mollusk group. We confirm the general findings of Nudelman et al. (2006), now for *H. rufescens*,

* Corresponding author. Fax: +1 858 534 6373.
E-mail address: rasaro@ucsd.edu (R.J. Asaro).

1047-8477/$ - see front matter © 2008 Elsevier Inc. All rights reserved.
doi:10.1016/j.jsb.2008.04.009

but extend the structural characterization by focusing as well on the location of chitin within the framework. Our findings concerning chitin provide an important, and previously not understood picture of the organic framework that has specific implications to the mechanical and structural performance of the shell.

Several mollusk shells, such as that of *H. rufescens*, contain an outer prismatic (calcitic) layer (see *e.g.* Simkiss and Wilbur, 1989 or Zaremba et al., 1996) and an inner nacre. The nacreous portion is a biomineralized structure in which quasi-hexagonal $CaCO_3$ (aragonite) tiles are layered between, and bound to, a thin biopolymer protein framework secreted by epithelial cells (*e.g.* Simkiss and Wilbur, 1989; Belcher and Gooch, 2000; Addadi et al., 2006; Rousseau et al., 2005). The structure and crystallography of the ceramic tiles mollusk nacre have been studied *via* X-ray diffraction, SEM, TEM and AFM (see *e.g.* Wada, 1961, 1968; Wise, 1970; Crenshaw and Ristedt, 1976; Mutvei, 1979; Weiner et al., 1983; Sarikaya et al., 1995; and Manne et al., 1994). Tiles are crystallographically textured aragonite with a thickness in the range 300–500 nm and diameters in the range 4–10 μm. Nacre tiles are arranged in nearly parallel lamellae separated by thin *interlamellar layers* of biopolymer framework with a thickness in the shell of approximately 30 nm (*e.g.* Checa and Rodriguez-Navarro, 2005) . Within each lamella the tiles grow laterally and meet at what become polygonal boundaries separated by an *intertabular matrix*; examples are shown below. Nacre tiles often respond, *via* diffraction, as single crystalline tablets but are known to contain an organic intracrystalline matrix. Recently, for example, Rousseau et al. (2005) have performed AFM imaging, in tapping mode, and TEM dark field imaging of nacre tablets in the oyster *Pinctada maxima* and provided evidence for a continuous intracrystalline matrix surrounding coherent nanograins that comprise individual tablets. Their results suggest, among other things, a pathway for modeling the mechanical response of nacre that we use below in suggesting a preliminary model for the interlamellar layers. Likewise, Oaki and Imai (2005) describe a hierarchical structure of nacre in the pearl oyster *Pinctada fucata* in which individual tiles are seen to be composed of nano-scale "building blocks" (*i.e.* nano-crystals) surrounded by an organic matrix (*i.e.* the intracrystalline matrix). The AFM images shown by Rousseau et al. (2005) can be used to demonstrate that the stiffness of individual tiles should be less than that of monolithic $CaCO_3$ and, in fact, just on the basis of a simple rule of mixtures should be on the order of at least 10% less. This estimate is based on the apparent thickness of the intracrystalline matrix as seen, for example, in the phase image of Fig. 3b of Rousseau et al. (2005). At the same time, the intracrystalline matrix would impart increased toughness to the structure *via* the energy absorptive capability of a visco-elastic matrix.

The biopolymer framework has previously been studied primarily through optical microscopy (*e.g.* Crenshaw and Ristedt, 1976; Gregoire, 1957, 1972) and biochemical studies of amino acid composition (see *e.g.* Wheeler and Sykes, 1984; Cariolou and Morse, 1988; Simkiss and Wilbur, 1989; Addadi and Weiner, 1985 and Aizenberg et al., 1999). Quite limited study using either TEM (Weiner et al., 1983; Levi-Kalisman et al., 2001) or AFM (Schaffer et al., 1997; Manne et al., 1994; Rousseau et al., 2005) has been performed to date; only the latter was performed on *H. rufescens* . As is well established, the matrix associated with nacre tissue is approximately 75–80 wt% protein and balance carbohydrate with some glycoproteins (see *e.g.* Addadi and Weiner, 1985). Our own assays are consistent with this and a typical amino acid analysis shows that our *H. rufescens* insoluble nacre framework contains residues that are rich in Asp and Glu and are acidic as reported by others. Approximately 20% of the residues are Asp and 4% Glu. There have been reports of chitin in the framework of several mollusks other than *H. rufescens* (Weiner and Traub, 1980, 1984; Weiner et al., 1983; Poulicek, 1983; Goffinet and Jeuniaux, 1979; Zentz et al., 2001) but until our assays, to be reported herein, were completed no truly definitive and quantitative evidence for chitin had existed in *H. rufescens*; reasons for this stem from, in particular, difficulties in properly hydrolyzing the complete framework prior to analysis. We have, however, recently succeeded in performing an accurate analysis with the interesting result that for the as extracted insoluble framework we find 6.4 wt% chitin, whereas in the extracted framework subjected to digestion with trypsin the content is higher at 6.9 wt%. This is a remarkably high chitin content even when compared to that found in fungal cell walls (Ruiz-Herrera, 1992; San-Blas and Calderone, 2004), and more specifically as compared with the much lower contents reported by Poulicek (1983) in gastropods. Our assay is, however, consistent with the chitin contents reported by Goffinet and Jeuniaux, 1979 for other mollusk species. There are soluble proteins that are removed during demineralization and some have been isolated, (see *e.g.* Belcher et al., 1996). They too are rich in Asp and Glu, bind Ca^{++}, and can play a vital role in mineralization (Falini et al., 1996; Belcher et al., 1996; Addadi et al., 2001; Gotliv et al., 2003).

Of particular interest is the structure of the $CaCO_3$ nucleation sites. Crenshaw and Ristedt (1976), following Crenshaw (1972), used the fact that once demineralized, the interlamellar matrix reveals the outlines of the tiles, and mapped the location of sulfates, carboxylates, and calcium binding sites within them. Wada (1980) later confirmed the presence of high concentrations of sulfur in the central region, thus suggesting that the nucleation site was located there. Here, we use AFM methods combined with histochemical fluorescent microscopy to map such structure in *H. rufescens* and include chitin within our maps. Our mapping is then used to confirm and extend models for nacre growth and for developing an approach to modeling the shell's mechanical properties. This provides the path to biomimetics and bio-duplication of synthetic materials.

2. Materials and methods

2.1. Materials

Fresh shells of both *H. rufescens* and *N. pompilius* were obtained from The Abalone Farm Inc. of Monterey, CA and were stored dry at 4 °C. The nacreous portion of the shells were removed by slowly grinding off the prismatic (outer) part and then washing the nacre sections in deionized water (DI). Sections varied in size, but often were up to 20 × 20 mm in cross section and up to 2 mm thick. For the tensile specimens described in Section 4, the sections were larger and up to 40 mm long. Fifteen live *H. rufescens* were also provided by the Abalone Farm Inc. and were kept in large tanks with continuously running sea water at the Scripps Institution of Oceanography at UCSD. These were used for the making of "flat pearls", *inter alia*, as shown in Fig. 1c. Flat pearls were prepared by inserting 5 mm glass slides under the mantle of live *H. rufescens* and allowing approximately three weeks for nacre to form. The slides were then removed and washed in DI.

2.2. Demineralization

After washing in DI, shell sections were demineralized either in Ethylene Diamine Tetraacetic Acid (EDTA, Sigma), or by cation-exchange resin (Dowex 50 W × 8 50–100 mesh, Sigma). Demineralization was carried out at 20 °C for times that depended on the method and on the size and thickness of the shell fragments. Decalcification by ion exchange resin was adapted from Gotliv et al. (2003). Nacre fragments were placed in sections of dialysis tubing (MWCO 3500, 19 mm flat width, Fisher). Unfixed samples were placed in dialysis membranes filled with DI water while fixed samples were placed in dialysis membranes containing a 4% formaldehyde, 0.5% cetylpyridinium chloride (CPC) solution. 10 mm long

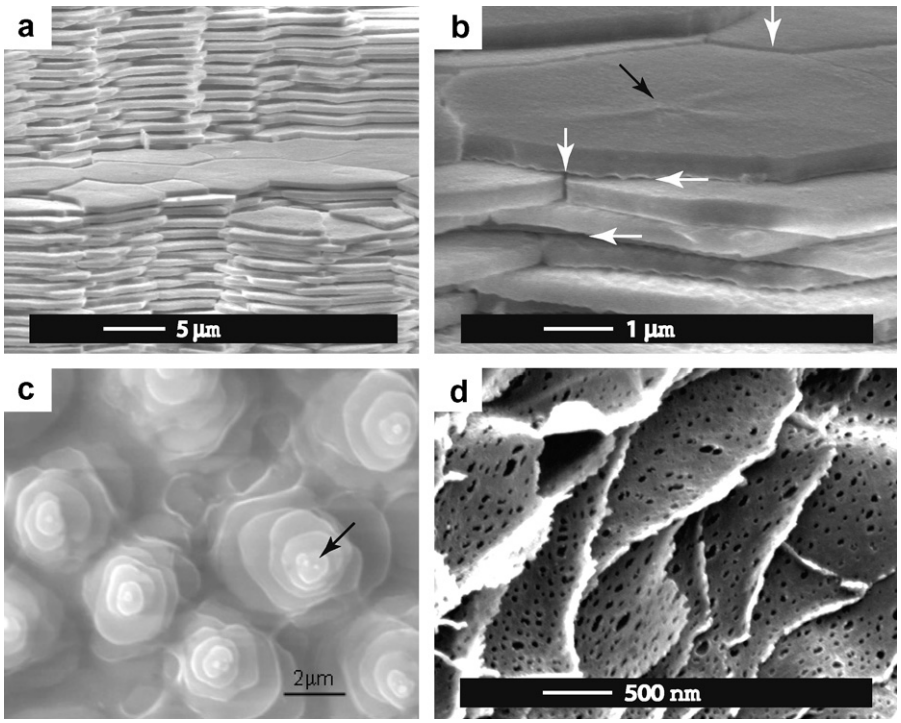

Fig. 1. (a and b) SEM images of fractured nacre from *H. rufescens* illustrating tiles on nearly parallel lamella. The "terrace" consisting of one interlamellar layer of nacre is shown at higher magnification in (b), where the black arrow points to a central region discussed below and referred to in Mutvei (1979). (c) Flat pearls grown on a glass slide inserted into the mantle of a live red abalone (described below). Note the "stack of coins" arrangement with a smaller tile (or tiles) nucleated at the top of each stack. (d) SEM image of a cross section of *H. rufescens* organic matrix, demineralized in EDTA, illustrating individual and apparently porous interlamellar layers.

sections of tubing containing unfixed specimens were placed in 4 l of DI containing 750 ml of pre-washed resin. A stir bar was used to keep the resin in constant suspension at room temperature and the water was replaced once a day. Decalcification was verified by infrared spectroscopy. Fixed samples placed in sections of dialysis tubing were allowed to demineralize in 50 ml conical tubes filled with 15 ml of resin and topped off with the formalyn/CPC solution. The tubes were placed on a tilt platform such that the resin remained in suspension during decalcification. The demineralization was complete after 1–4 weeks. For starting fragments with a thickness of approximately 0.5 mm, typically 1 week–10 days was sufficient. Thicker fragments, *e.g.* those with thickness up to 1 mm, required the longer times. Following Crenshaw and Ristedt (1976), decalcification using EDTA was performed by placing nacre fragments in 50 ml conical tubes filled with 1 M EDTA, pH 8, at room temperature under gentle shaking. Samples were also decalcified in EDTA containing 4% formaldehyde and 0.5% CPC (Williams and Jackson, 1956). After demineralization, all samples were extensively washed in DI water to remove any remaining EDTA, formaldehyde or CPC. Interlamellar sheets were separated using fine tweezers under an optical microscope. Demineralization times ranged from 1 week to 10 days depending on the thickness of the starting fragment.

2.3. Enzymatic digestion

2.3.1. Trypsin

Ten microgram of wet interlamellar sheets were incubated for 24 h at room temperature in 0.1 M ammonium bicarbonate buffer, pH 8.0, containing 1 mg/mL trypsin (Invitrogen).

2.3.2. Proteinase-K

Following Schaffer et al. (1997), interlamellar sheets of demineralized shell were sonicated for 10 min in 1 mL of 5 mM Hepes buffer, pH 7.5. The samples were then centrifuged at 12,000 rpm for 10 min in an Eppendorf centrifuge. The supernatant was removed and replaced by 1 mL of Hepes buffer containing 200 µg/mL proteinase-K (Sigma). The pellets were sonicated in this solution for 10 min and left to incubate for 2 h at room temperature. The samples were then centrifuged for 10 min at 12,000 rpm. The supernatant was removed and the pellets were washed with Hepes buffer.

2.3.3. Collagenase

As described in Schaffer et al. (1997), sheets of demineralized tissue were incubated for 2 h in 1 mL of 200 µg/ mL collagenase combined with 200 µM $CaCl_2$ in 5 mM Hepes buffer, pH 7.5. Samples were centrifuged for 10 min at 12,000 rpm and sonicated in DI for 10 min.

2.3.4. N-Glycosidase F

N-Glycosidase F (PNGase F, New England Bio Labs, P0704S) is an amidase that cleaves between the innermost glucosamine and asparagine residues of numerous N-linked glycoproteins. One centimetre square sections of demineralized tissue were separated into approximately 1 µm thick, interlamellar sheets. The sheets were incubated in 1 µL of 10 × glycoprotein denaturing buffer and DI water to make a total reaction volume of 750 µL. The samples and buffer were combined in 1.5 mL centrifuge tubes. The tubes containing the samples were placed in water heated to 100 °C for 15 min. A total reaction volume of 20 µL was prepared by adding 2 µL of 10 × G7 reaction buffer, 2 µL of 10% NP40, 2 µL *N*-Glycosidase F, and 14 µL of DI water. The samples were incubated at room temperature in this solution for 2 h.

2.4. Staining methods

2.4.1. Calcofluor white

Calcofluor white (CW) is a fluorescent brightener that binds to β-1-3 and β-1-4 polysaccharides as are found in cellulose and

chitin, respectively (Maeda and Ishida, 1967; Peters and Latka, 1986; Hayat, 1993; Harrington and Hageage, 2003). Staining of demineralized tissue was performed as follows. A 10% potassium hydroxide reagent was prepared by dissolving 10 g of KOH in 90 mL of DI water to which 10 mL of glycerin were added. A second CW reagent was prepared by dissolving 0.1 g of fluorescent brightener 28 (Sigma) in 100 mL of DI water under gentle heating. Interlamellar sheets, approximately 1–2 μm thick were mounted on slides. Two drops of each reagent were added to the samples. After 4 min the samples were rinsed in water, air dried and mounted in Entellan mounting medium(Merck).

2.4.2. Colloidal iron

Colloidal iron staining was performed following methods outlined in Pearse (1968). Stock colloidal iron solution was prepared by stirring in 29% ferric chloride to boiling water. Once the solution turned dark red it was allowed to cool to 20 °C. The solution was then dialyzed three times for 24 h against a volume of DI 5× that of the stock solution. The reagent was stored at 20 °C. The working colloidal iron solution, pH 1.8, had a shelf life of 24 h. This solution consisted of DI, glacial acetic acid, and stock colloidal iron solution combined at a ratio of 18:12:10. As in Nudelman et al. (2006), the tissue samples were submerged in the working solution for 1 h, rinsed thoroughly with 12% acetic acid, incubated with 5% potassium ferrocyanide/5% HCl (1:1) for 20 min, and washed with water. Samples were mounted as described above.

2.4.3. Aminoacridone

Following Nudelman et al. (2006), thin layers of interlamellar tissue were incubated in 1% *N*-(3 dimethylaminopropyl)-*N′*-ethylcarbodiimide hydrochloride (EDC) in a 20 mM phosphate buffer at pH 4.5. The samples were washed three times with 0.2 M borate buffer, pH 8.5, and incubated for 12 h in aminoacridone (1 mg/100 ml) in the borate buffer. The samples were rinsed with water and mounted as described above.

2.5. Wheat germ agglutinin–colloidal gold (WGA–gold)

2.5.1. Probe preparation

Wheat germ agglutinin (WGA) is a lectin that binds to sequences of three β-1-4 linked *N*-acetyl-D-glucosamine residues as well as to sialic acid residues. As a result WGA has a high affinity to chitin and to a lesser extent to some glycoproteins. Colloidal gold can be complexed to WGA for the purpose of locating chitin on the biopolymer layer remaining after shell demineralization. Colloidal gold particles typically used for high resolution TEM studies can be enhanced using silver enhancement reagents. This allows for the imaging of these particles using standard SEM and optical microscopic techniques. Our procedures were closely adapted from King et al. (1987) and Geoghegan and Ackerman (1997). WGA–gold complexes were prepared as follows. 0.75 mg WGA in 1 μL of distilled water were combined with 25 mL of colloidal gold, pH 9.9. The gold particles were of a nominal size of 10 nm(Sigma). The complexes were stirred for 3 min after which 1% polyethylene glycol (PEG) was added. After 5 min the reagent was centrifuged at 60,000*g* in a Beckman ultracentrifuge for 1 h at 4 °C. The supernatant was removed and the sedimented WGA–gold complexes were resuspended to 5 mL with phosphate buffered saline (PBS) pH 8, containing 0.2 mg/mL of PEG.

2.5.2. Labeling procedure

Fixed and unfixed interlamellar tissue was sectioned into 1 cm^2 approximately 1 mm thick. Samples were incubated in the WGA–gold complexes for 30 min. The WGA–gold complexes were used at a dilution of 1:100 in PBS, pH 7.0. After labeling the samples were washed in six changes of PBS, pH 7.2.

2.5.3. Silver intensification

Aurion SE-EM silver enhancement reagent(Aurion) was prepared immediately before use. Samples treated with WGA–gold complexes were rinsed in DI water three times and placed in the enhancing reagent for 4 min after which they were washed in five changes of DI water.

2.5.4. Cytochemical controls

The specificity to chitin of WGA–gold complexes was determined by pre-incubating the complexes in *N*,*N′*,*N″*-triacetylchitotriose. Another set of samples was incubated in unlabeled WGA (0.5 mg/mL). Specificity to chitin was further determined by a comparative analysis using FITC-WGA(Molecular Probes) and CW which binds specifically to β-1-3 and β-1-4 glucosides *i.e.* cellulose and chitin, (Maeda and Ishida, 1967; Peters and Latka, 1986; Lukes et al., 1993). Of these two polysaccharides, chitin is the only one which is labeled by both WGA and CW.

2.5.5. Fluorescein-WGA

Following El Gueddari et al. (2002), interlamellar sheets were incubated with 2% w/v bovine serum albumin (BSA) in PBS for 30 min at 20 °C. Samples were washed three times with PBS/Tween20 and incubated in FITC-WGA(0.1 mg/mL in PBS, 1% w/v BSA) for 1 h. Samples were washed three times with PBS/Tween20, washed once in DI water, air dried on glass cover slips, and mounted in Entellan.

2.6. Scanning electron microscopy

Samples were dehydrated in an ethanol series and critical point dried with liquid carbon dioxide. Samples were mounted with carbon tabs and sputter coated with 15 nm of chromium. Samples were immediately examined using a Philips XL30 ESEM operated at 10 kV.

2.7. Immunohistochemistry

Gotliv et al. (2003) produced polyclonal antibodies raised against soluble aragonite-nucleating proteins from the bivalve *A. rigida*. The proteins were earlier found to nucleate aragonite by Falini et al. (1996). Nudelman et al. (2006) found positive labeling with these antibodies in both *A. rigida* and *N. pompilius* and consequently to explore the possibility of similar effects in *H. rufescens* we used similar immunohistochemical labeling procedures. Polyclonal antibodies were generously supplied to us by S. Weiner (2007).

Interlamellar sheets from *H. rufescens* were incubated in serum containing polyclonal antibodies for 1 h. The serum was diluted 1:25 in PBS containing 0.25% w/v BSA to block non-specific binding. The samples were washed twice for 5 min with PBS containing Tween20(0.05% w/v). Samples were then incubated for 40 min in the secondary antibody, rhodamine conjugated goat-anti-rabbit(Jackson ImmunoResearch, diluted 1:100 in PBS). Before imaging the specimens were washed three times for 5 min with PBS and Tween20(0.05% w/v) to remove unbound antibodies. After rinsing the samples in DI water, the samples were air dried on cover slips and mounted in Entellan. As a control, samples incubated in a pre-immune serum were prepared as above.

2.8. Optical microscopy

Samples were observed using a Nikon Eclipse 80i optical microscope equipped with a Photometrics CoolSNAPez digital camera. Calcofluor white and aminoacridone-stained samples were viewed using a 11003 V3 filter set, while samples labeled with FITC and rhodamine where viewed using a 41001 filter set(Chroma).

2.9. Chitin assays

Our method was based on the evaluation of glucosamine content found in demineralized tissue samples. 1 mg of tissue (dry weight) was resuspended in 1 ml of 6 M HCl and hydrolyzed at 100 °C for 17 h, together with *N*-acetylglucosamine (GlcNAc) as a standard. Samples were then dried and resuspended in 1 ml DI water. The quantity of glucosamine released by the hydrolysis of 100 μL of this material was determined as follows. An equal volume of 4% (v/v) acetylacetone in 1.5 M Na_2CO_3 was added, and the preparation heated at 100 °C for 20 min. Samples were then diluted with 700 μL 96% ethanol and incubated for 1 hr at 23 °C, after 100 μL Ehrlich's reagent (1.6 g/ml *p*-dimethylaminobenzaldehyde, 6 M HCl, 50% ethanol) was added. Samples were incubated for 15 min at 65 °C before the absorbance was read at 520 nm.

2.10. AFM methods

Atomic force microscopy (AFM) techniques were used to characterize the protein network structure of decalcified abalone shells. Intermittent contact (tapping) mode of operation was used to obtain both surface topographic and phase information. In tapping mode, the "diving board" shaped, low force-constant cantilever, which has a very sharp silicon tip located at the end on the bottom side, is oscillated at its resonance frequency by a piezoelectric element located on the cantilever holder, which is mounted on a piezoelectric tube scanner. This intermittent contact mode of operation and low force-constant cantilevers were originally developed specifically to minimize damage to soft, easily damaged samples. A laser beam, focused onto the backside of the cantilever end, is reflected *via* an adjustable mirror onto an optical sensor. As the cantilever tip is rastered back and forth over the sample surface, variations in sample height result in deflection of the cantilever from its rest position. These deflections cause variations in the optical sensor signal that are converted to a voltage that is applied to the z electrode of the scanner, causing it to expand or contract, and thus raise or lower the cantilever back to its undeflected position. Since the changes in the scanner dimensions are calibrated in nanometers per volt, the changes in applied voltage are mapped as local variations in sample height superimposed on an *x*-*y* grid (scan size) set by the user. The sharp tip allows one to obtain nanometer resolution of surface features.

Typical resonance frequencies for the commercial AFM cantilevers (NanoDevices, approximately 125 μm long × 45 μm wide × 4 μm thick) used in this study were around 300 kHz. In addition to monitoring changes in the cantilever deflection position, simultaneously phase imaging, which captures the phase lag angle between the drive signal and actual cantilever oscillation, was used to obtain maps of variations in local properties such as stiffness. Therefore there is a one-to-one correlation between the topographic data and the corresponding phase information.

The AFM is equipped with a special cantilever wet cell holder, which was used to image samples under *in vitro* conditions. Samples were mounted on steel pucks that are held in place on the AFM sample stage by a magnet buried in the base. Since the hydrated samples could not be fixed to the sample by tape, samples were cut large enough to be held in place using the wet cell o-ring seal. Only thin continuous sections were used for imaging to prevent small sections from coming lose during imaging and interfering with the imaging process. Ambient imaging was used for dried and stained samples. In all cases, tapping mode imaging was used. We used Veeco Metrology Nanoscope IIIa controllers with a D3000 microscope to image the dried samples and a Multimode microscope for the wet cell imaging.

2.11. Mechanical properties and modeling

Specimens were "dog bone" type and were machined from polished flat sections of the nacreous parts of whole shells. Steel templates were first made of the specimens to ensure dimensional uniformity across the gauge section and the machining was performed *via* slow grinding to minimize damage to the edges. The gauge sections were 14 mm in length, 2 mm wide, and 0.5 mm thick. Axial strain was measured using an extensometer with a resolution in strain of approximately 5×10^{-6}. Testing was performed in an Instron 5565 material test system, in stroke (*i.e.* displacement) control; this system has a mechanically controlled cross head and thus is extremely stable. Axial strain rates ranged from 10^{-3} to -10^{-4}. Modeling was performed for the purpose of extracting estimates for the shear stiffness of the interlamellar layers using a "shear lag" analytical model that has been verified by finite element analysis.

3. Results

3.1. SEM observations

The following SEM observations are briefly described most particularly to provide additional perspective on the structure of nacre in our *H. rufescens*. Fig. 1a and b shows SEM images of the tile cross-section of a fractured shell that illustrate the optimal interdigitated nacre brick-wall structure. Additional description of the structure, including the interlamellar and intertabular layers may be seen in the images and are described in the caption. Interlamellar regions are identified by the horizontal white arrows in Fig. 1b; the intertabular regions are identified by the vertical white arrows. The black arrow indicates a central region observed in all tiles which had been referred to earlier by Mutvei (1979). Fig. 1d shows an image of individual demineralized interlamellar layers of the external organic matrix. Such images were obtained from critically point dried matrix tissue and show thickness in the range 80–100 nm; in the shell the interlamellar layers are 30 nm as just noted. The layers appear porous in Fig. 1d and this will be further elucidated when our AFM results are shown later. Fig. 1c shows the growth of "flat pearls" grown on the surface of glass slides inserted under the mantle of live *H. rufescens*; such observations will be referred to in our discussion of nacre growth. A noteworthy feature of the flat pearls is the appearance of more than one tile nucleated atop a tile growing laterally on a layer just below. An example of such multiple tile nucleation is indicated by the black arrow in Fig. 1c.

3.2. Optical histochemical microscopy

3.2.1. Calcofluor white staining

Calcofluor white is a fluorophore that binds to glycans and fibrillar polysaccharides such as chitin (*e.g.* Herth, 1980; Ramaswamy et al., 1997). Organic matrices from *H. rufescens* were stained and imaged after demineralization in EDTA and by cation-exchange resin. In both cases strong binding was detected as shown in Fig. 2c and d. For perspective, however, we first show SEM images of demineralized nacre taken normal to the interlamellar plane, Fig. 2a and b. These images may be compared to those reported by Mutvei (1979, 1977), where similarities and differences may be noted.

As in Mutvei's (1977) SEM images, the intertabular matrix, surrounding the tiles, is clearly revealed as is the appearance of an evidently organic ring-like structure organized around what was the tiles' centers. Etching, in the form of "pits", occurs throughout the surface of the interlamellar layers, but we do not observe the

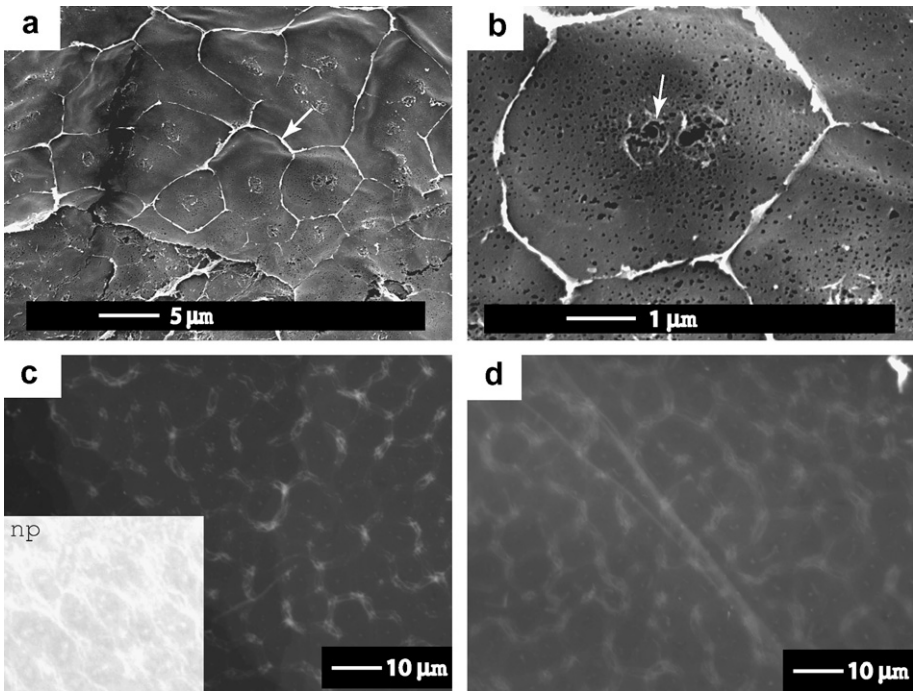

Fig. 2. (a and b) are SEM images of demineralized organic framework in *H. rufescens*. Note that the center of each tile imprint is more deeply etched; the apparent accumulation of organic material at the center. (c) An epi-fluorescent micrograph of *H. rufescens* stained with CW following demineralization in EDTA. The insert is of *N. pompilius* demineralized and stained in the same manner. (d) Same as (c) except with demineralization with ion exchange. The lower contrast in (d) is due to a low exposure time of 300 ms.

radial organic membranes reported by Mutvei (1977) in his study of the gastropod *Gibbula*. The interlamellar layers at locations of the tile centers typically etch deeply indicating an organic/mineral accumulation there as reported by Mutvei (1979, 1977). The centers of the lamellar layers appear to contain significant amounts of mineral that is removed rapidly by both EDTA and ion exchange along with organic material that is exposed by the demineralization process. As mineral is removed, and organic material is exposed, the appearance of the latter is that of a "ring-like" structure. Fig. 2c and d shows the effect of CW staining on *H. rufescens*; the insert in Fig. 2c is an additional image obtained from *N. pompilius* showing a similar pattern of staining as for *H. rufescens*. Strong binding of CW is observed at the intertabular matrix in both cases and, at a lesser intensity, at the very center of the tiles. The center illumination is not in the form of a ring-like structure, but rather appears as a quite localized area of CW binding. This evidence, combined with supporting results using WGA–gold and FITC-WGA conjugates, indicates that these locations contain significant amounts of chitin.

We note that the staining at the intertabular matrix often appears in the form of a "double-layer" as, for example, in Fig. 2c. This might suggest the possibility of a two layered structure recently described by Marin et al. (2007) in the bivalve *Pinna nobilis*. We believe, however, that in this case the structure is caused by the physical topography of the intertabular matrix as shown and described below.

3.2.2. WGA–gold staining

Fig. 3a–c shows optical images of *H. rufescens* obtained after demineralization with EDTA and labeled with WGA–gold; Fig. 3d is enhanced with fluorescein conjugated to WGA after demineralization in EDTA and digestion with PNGase F. Distinct staining is evident on the intertabular matrix with heavy accumulations of colloidal gold seen outlining, in many cases, complete intertabular boundaries. Labeling of fibrous structures is also seen within the tile imprints as is most evident in Fig. 3c (see the white arrow). In many cases the "fibers" of such structures are seen to emanate out from the intertabular matrix as indicated by the arrows in Fig. 3b. The diameters of the fibers was only approximately determined and appear to lie in the range of ~30 nm. Fluorescein staining, shown in Fig. 3d, reveals again the strong labeling of the intertabular matrix and the pattern of projection of structure emanating from it. Later we present evidence of a chitin core and suggest that the lighter staining with CW at the center is due to exposure, and not an excess accumulation, of chitin beneath the protein layers of the framework. Referring back to Fig. 2c and d we now suggest that the lighter staining with CW at the center described there was due to the exposure, and not an excess accumulation, of chitin beneath the protein layers of the framework.

3.2.3. Aminoacridone staining

Aminoacridone is a fluorescent compound that binds to carboxyl groups in the presence of carbodiimide (EDC). *H. rufescens* tissue, demineralized in EDTA, was imaged in both the fixed and unfixed states as shown in Fig. 4a and b, respectively. As the samples are observed in epifluorescence, labeling appears white in the images. The unfixed samples showed labeling in the intertabular matrix, but little or no labeling was observed within the tile imprints and, in particular, at the center of the tiles, Fig. 4. This is in contrast with results reported by Nudelman et al. (2006) for *N. pompilius* who reported definite labeling at the center region for unfixed samples. On the other hand for fixed samples, Fig. 4a, labeling was observed albeit faint (see insert and the white arrow head) as also noted by Nudelman et al. (2006) for *N. pompilius*. The central regions typically appeared dark, and in fact black in the unfixed samples. We suspect from this that we were not suffering from possible artifacts caused by residual EDTA as noted by Nudelman et al. (2006) and by, for example Wheeler et al. (1987). Very low levels of fluorescence were detected in regions between the center and the intertabular regions. For further confirmation of

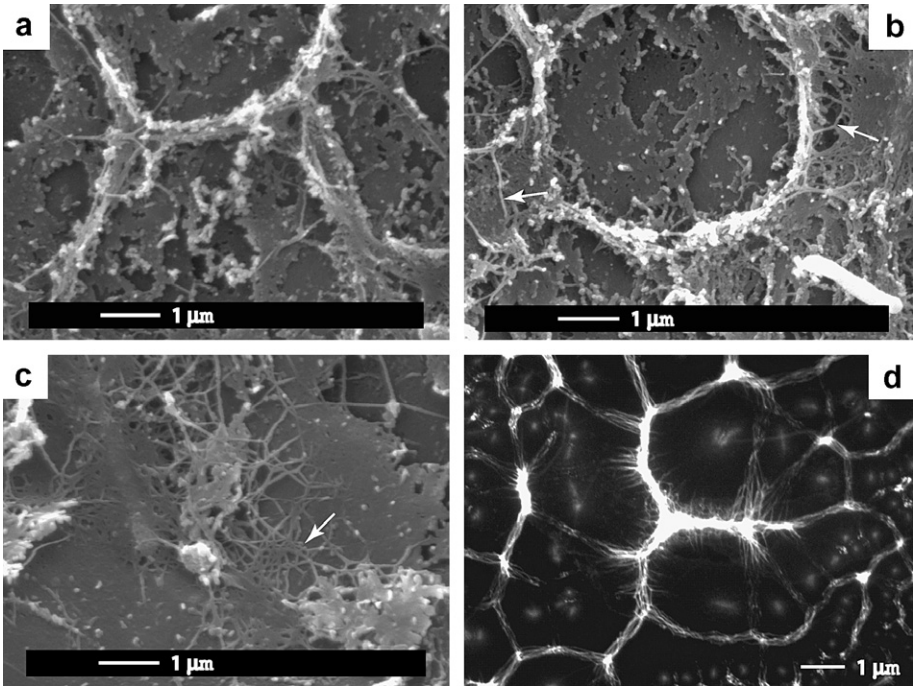

Fig. 3. (a–c) are images obtained after demineralization with EDTA, without fixing, and labeled with WGA–gold. Strong labeling of the intertabular matrix is evident as is the appearance of a fibrous network (small arrow heads in (b) and (c)). Gold labeling appears white in (a–c). (d) Epifluorescence of an EDTA demineralized sample, digested, with PNGase F, and stained with FITC-WGA.

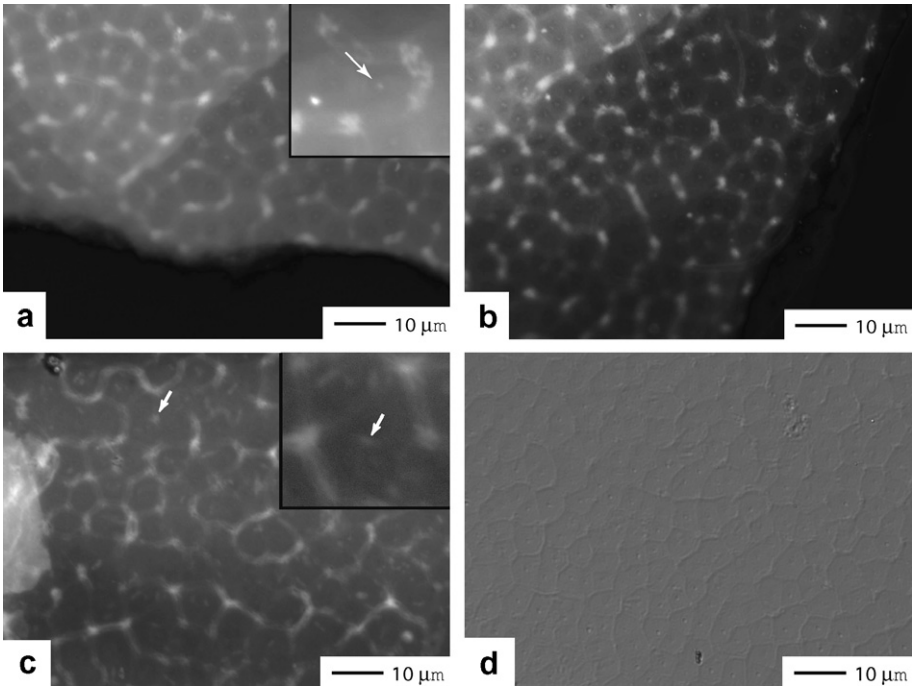

Fig. 4. (a) Epifluorescenct images of *H. rufescens* demineralized using EDTA, fixed, and stained with aminoacridone. (b) Unfixed *H. rufescens* imaged after staining. Note the faint but distinct labeling at the center in the fixed sample, shown more clearly in the insert to (a). (c) Epifluorescenct images of *H. rufescens* demineralized using ion exchange, fixed, and stained with aminoacridone. The white arrows indicate staining at the center of tile imprints. (d) Bright field image of *H. rufescens* demineralized using ion exchange.

our images being artifact free, we stained and imaged samples demineralized using ion exchange; a typical example for a fixed specimen is shown in Fig. 4c. The images are quite similar to those obtained with fixed samples demineralized in EDTA. Staining was observed at the intertabular matrix and at the tiles' centers (see insert and arrows). For reference we show a bright field image in Fig. 4d. We had used such images to compliment our infrared spectroscopy to assess the degree of demineralization and to view the general topography of the tissue samples. We judged the sample as shown in Fig. 4d to be demineralized, but we note that additional

care was required to assess the completeness of demineralization *via* ion exchange.

3.2.4. Colloidal iron staining

Staining with colloidal iron is commonly performed to label acidic polysaccharides *via* the binding of iron to charged acidic groups, including carboxylates and sulfates. To distinguish the labeling of sulfates from carboxylates, staining is done at a pH low enough to protonate the carboxylates. Thus our staining was performed at a pH 1.8, so that only sulfates were labeled. Strong labeling was observed within ring-like structures in the center of the tile imprints, as clearly seen in both Fig. 5a and b. In fact, the stained ring-like structures are most pronounced in *H. rufescens* demineralized in EDTA and unfixed contrary to other reports, *viz.* Crenshaw and Ristedt, 1976; Nudelman et al., 2006, concerned with *N. pompilius*, that note the lack of labeling in unfixed samples. Still another feature that contrasts with the later's findings is the near absence of labeling in the intertabular matrix. The ring-like structure of those regions believed to contain acidic sulfates is, however, in agreement with the results and conclusions of Nudelman et al., 2006, concerning similar structure in *N. pompilius*.

Samples were also demineralized and digested with trypsin + proteinase K, stained and imaged. Fig. 5c and d shows results following staining with colloidal iron and CW, respectively. Labeling by colloidal iron was essentially eradicated after digestion indicating that the macromolecules responsible for colloidal iron binding were removed. On the other hand, labeling of the intertabular regions and in the center regions by CW was hardly affected.

3.2.5. Immunohistochemical staining

Acidic proteins containing high concentrations of aspartic and/or glutamic acids are an integral part of the organic matrix as already noted. Acidic polysaccharides, including some that are sulfated have also been identified. Falini et al. (1996) and Gotliv et al. (2003) have isolated such acidic macromolecules that they showed helped nucleate aragonite when introduced into an *in vitro* assembly of (*Loligo* β) chitin and (*Bombyx mori*) silk fibroin. Gotliv et al. (2003) isolated their matrix molecules from *A. rigida* and Nudelman et al. (2006) showed positive results on both *Atrina* and *N. pompilius* using polyclonal antibodies raised against these molecules. Here we apply the same immunohistochemical procedure to label the demineralized interlamellar/intertabular matrix of *H. rufescens* to explore the possibility that these mineral nucleating macromolecules may be present, and thereby aide in locating potential aragonite nucleating sites.

Fig. 6a and b shows that in *H. rufescens* labeling is quite sharp and highly localized as found by Nudelman et al. (2006) in both *A. rigida* and *N. pompilius*. Labeling is distinct at the intertabular matrix, and perhaps sharpest at the "vertex junctions" of the tile imprints. Labeling is also seen at the imprint centers as is especially clear in Fig. 6b. In fact, labeling of multiple sites within the interior of a tile imprint is often observed; this feature will be discussed in view of the already noted observation of multiple tile nucleation as observed in flat pearl nucleation and growth (see Fig. 1c). Fig. 6d shows a typical image from a sample treated with only pre-immune serum where no staining is detected at all. Our results are consistent with those of Nudelman et al. (2006), with the exception that they observe slight labeling of the intertabular matrix in *N. pompilius* with pre-immune serum. Fig. 6c is an image obtained with aminoacridone staining as shown earlier in Fig. 4, that is shown here for perspective. The patterns of staining are quite similar suggesting co-location of molecules rich in carboxylates and aragonite nucleating macromolecules. We note again the double-layer like structure (*e.g.* Fig. 6a and c) at the intertabular matrix that we attribute to the physical topography of this matrix.

3.3. AFM analysis

Both high and low resolution scans, in tapping mode, were performed over areas ranging from 500×500 nm up to 30×30 μm, the latter covering the range of our optical fluorescent views. Scans were made on specimens fixed and unfixed and with various degrees of digestion and/or staining. The images reveal fibrous structures characterized by at least two distinct size scales, the smaller

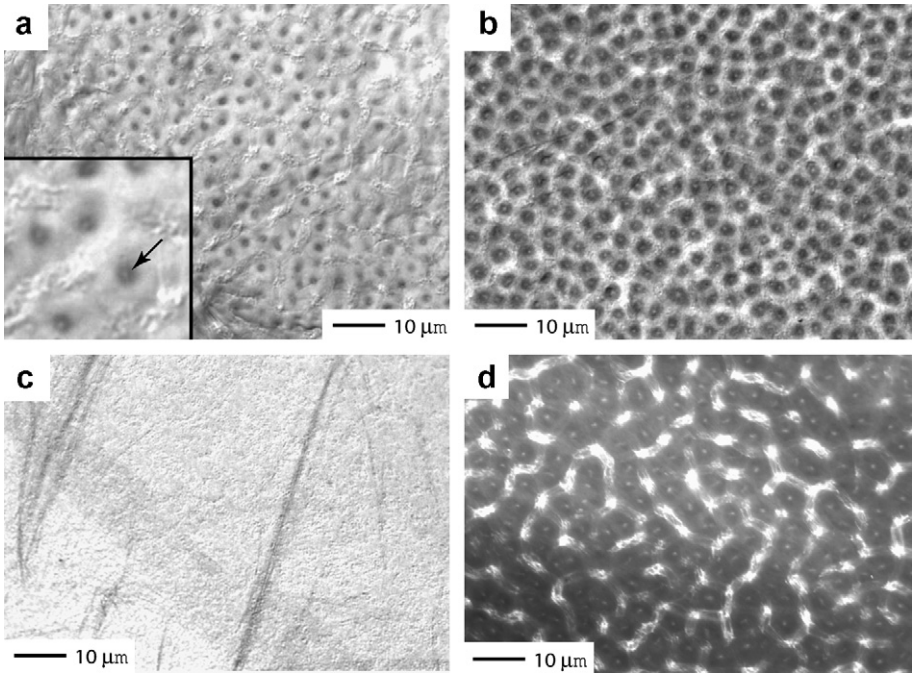

Fig. 5. *H. rufescens* stained with colloidal iron at pH in the range $1.8 \leqslant \text{pH} \leqslant 1.9$. (a) Demineralization performed using ion exchange and fixation. (b) Demineralization performed using EDTA and unfixed. (c) *H.* rufescens demineralized in EDTA, unfixed, and digested in Trypsin + proteinase K. (d) Same as (c) but stained with CW.

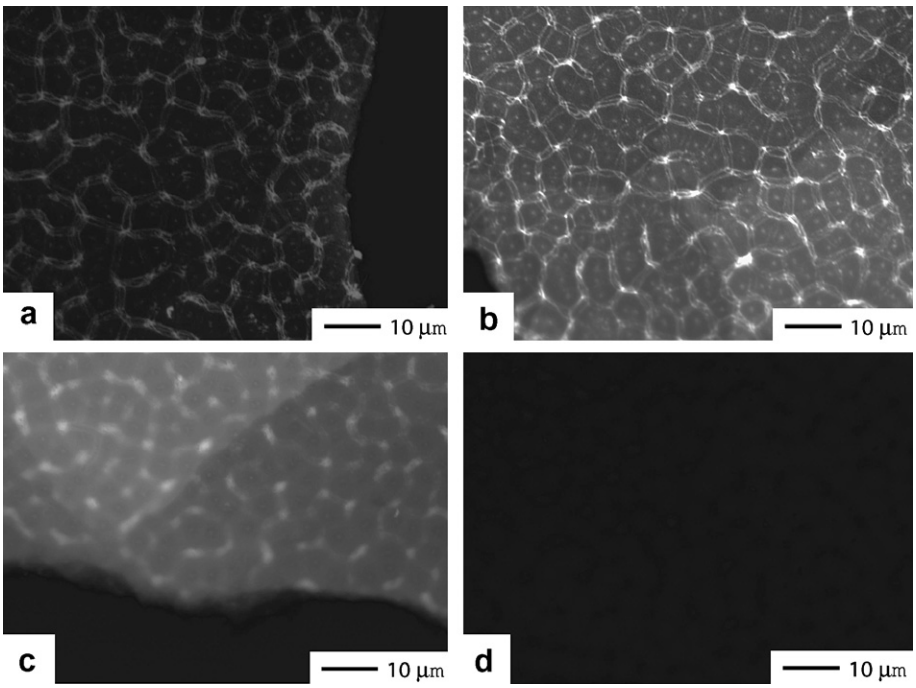

Fig. 6. (a and b) Images obtained from unfixed *H. rufescens*, demineralized with EDTA, and labeled with polyclonal antibodies. (c) An image obtained on a sample identical to that used in (a and b) using aminoacridone staining shown for perspective. (d) An image of unfixed *H. rufescens*, demineralized with EDTA, and labeled with pre-immune serum.

characterized by fibers, or fiber bundles, and the larger by an open network that creates pore-like openings.

Fig. 7 shows two typical scans over a larger area for an unfixed and undigested specimen of *H. rufescens* stained with calcofluor white. Fig. 7b shows a topograph image where Fig. 7a shows an elevation profile of that region. As in the histochemical images shown above, these large scans reveal the outlines of tiles on the surface of the organic interlamellar layers. Where the intertabular matrix has "collapsed", and where calcofluor white has evidently bound, the elevations can be as high as 250 nm above the locations of what were the tile/interlamellar layer interfaces. As we have determined that the tile diameter in our *H. rufescens* is 7 ± 0.5 μm, the images leave little doubt as to representing tile outlines. The central regions are depressed relative to the surrounding tile imprint as noted by the two central arrows. This depressed region is collocated with the central regions described in Fig. 2a and c where it is believed that mineral is preferentially removed during demineralization. What is also notable from the height profile of Fig. 7a is that the top edges of the intertabular layers are not flat but contain height differences of the order of 50 nm. This itself may account for the appearance of a "double layer" effect as discussed earlier in connection with Fig. 2c and d. As also noted above, the tile imprint centers are depressed, and the scans show these depressions are nearly 100 nm. The structure at the imprint centers is discussed below.

Fig. 8 are phase images of *H. rufescens* all obtained in tapping mode under fully hydrated conditions in a wet cell. Fig. 8a–c shows a progression of higher resolution scans of unfixed specimens digested with trypsin or trypsin + proteinase K. The lowest resolution scan of Fig. 8a, of a specimen that was digested in trypsin only, shows what appears to be a "porous" structure. Closer inspection, however, reveals embedded fibers (*e.g.* at the white arrow) and the fact that the layers contain a core of fibers. The fibrous core is more clearly revealed in Fig. 8b which is of a specimen digested in trypsin + proteinase K. Individual fibers are visible, and that they are embedded in less organized organic material is evident. Thus the interlamellar layers are not "porous" *per se* but are composed of a fibrous core, or network, that is embedded in and sandwiched between less organized organic material. Individual fibers appear to have diameters in the range 5–10 nm and run for lengths of at least 1 μm, although to date their length distribution has not been quantitatively determined. Fig. 8c shows a higher resolution scan which provides additional evidence of the fibrous network and suggests that the fibers may indeed be organized in nearly parallel bundles. In both fixed and unfixed samples there are examples where the fibers appear to be so organized, and examples that suggest a more random orientation. Our analysis of fiber orientation *via* 2D Fourier spectra, however, did not reveal long range order but did indicate short range order over distances of an imprint diameter. This would suggest that beneath a tile the fibers are ordered possibly as suggested by Weiner and Traub (1980). Fiber organization as observed here is also consistent with the recent observations of Rousseau et al. (2005) studying *P. maxima* who suggest that both the intracrystalline and intertabular matrices are highly organized. In the case of the intracrystalline matrix, they propose that it "reacts as a single crystal"; in the case of the interlamellar matrix, they conclude that it is "highly crystalized". Our observations such as shown in Fig. 8c and also Fig. 8d for *H. rufescens* are supportive of this proposal. Complete resolution, however, of the orientation distribution awaits further study.

Fig. 8d shows a phase image from a scan taken in a completely different orientation. Here a section of EDTA demineralized, unfixed and undigested, framework tissue was first mounted, edge-on, on a histology slide and sliced in a microtome so that approximately 1–2 μm of tissue stood nearly upright, *i.e.* nearly orthogonal to the glass slide; the orientation was much like that shown in the SEM image of Fig. 1d. The sections were, though, inclined to the vertical by about 30–40°, also consistent with the scenario of Fig. 1d. Specimens of this type were fully hydrated and scanned in tapping mode in a wet cell. The individual layers are evident and are hydrated so that their thickness is estimated (correcting for the angle of inclination) at ~80–120 nm. In the shell, the inter-

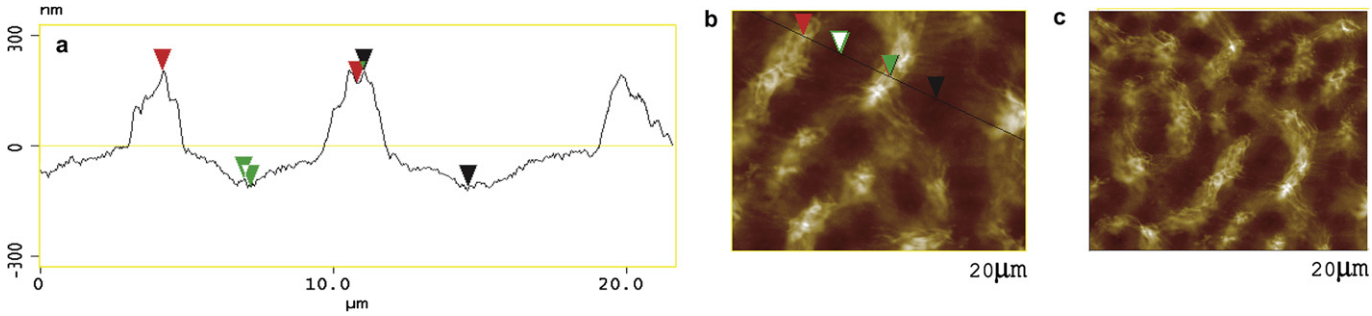

Fig. 7. (a) Elevation profile obtained from a large scan of *H. rufescens*, demineralized in EDTA, undigested, and unfixed. Scan formed in tapping mode, in water. (b) Topograph image accompanying (a) showing the elevations at the intertabular matrix. (c) Topograph similar to (b) from a different area.

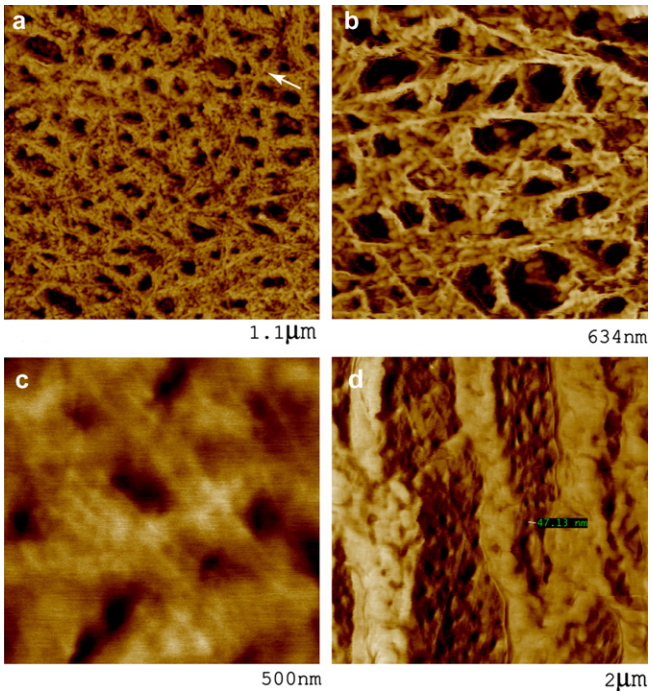

Fig. 8. (a–c) are phase images of intermellar sheets obtained in tapping mode from *H. rufescens* demineralized in EDTA, unfixed, and digested with (a) trypsin, (b and c) with trypsin + proteinase K. (d) phase image obtained in tapping mode of EDTA demineralized *H. rufescens*, unfixed, but mounted on a histology slide in a near edge-on orientation.

lamellar layers appear to be in the range ~30 nm in thickness, but demineralized tissue in water maintains a thickness of roughly that of the intact shell, *i.e.* it hydrates and swells by factors of approximately 3–4. Fibers are visible even in such undigested sections, and in fact on sections such as these appear to be arranged in an organized network. With reference to the staining of chitin with WGA as shown in Fig. 3 we suggest that the finer resolution of the fibers in the AFM images is due the residual amounts of organic matter surrounding the chitin fibers without, or with partial, digestion as used. In addition, the SEM specimens were Cr coated and this would also contribute to their appearing somewhat thicker. Fig. 9a and b shows results from a high resolution scan. The profile scan of Fig. 9a clearly illustrates the physical topography of the layers, including the intertabular matrix. Fig. 7a, associated with a much larger scan including at least two tiles, more clearly reveals the varying height profile across an intertabular zone. This sort of height difference, we believe, contributes to the patterns of staining described as "double-layers" earlier in images such as in Figs. 2a or 6a, for example. Fig. 9b is a phase image again showing the fibrous core that reveals "pores" about 40–80 nm in diameter that in our scans appeared to be about 10–20 nm deep. Fig. 9a is a height profile along the line shown in Fig. 9b; note the corresponding green and red markers in Fig. 9a and b. Profiles such as these indicate that variations in fiber height were in the range of less than a nanometer to up to 10 nm suggesting that they are not in the same plane. Moreover, there were instances where fibers appeared to run under and over other fibers suggesting the possibility of a weave like pattern. In some cases, such as shown in Figs. 8b and 9b, the fibers appear arranged more as a two dimensional scaffold analogous to the three dimensional chitin scaffold recently described by Miserez et al. (2008) within beak of the Humboldt squid

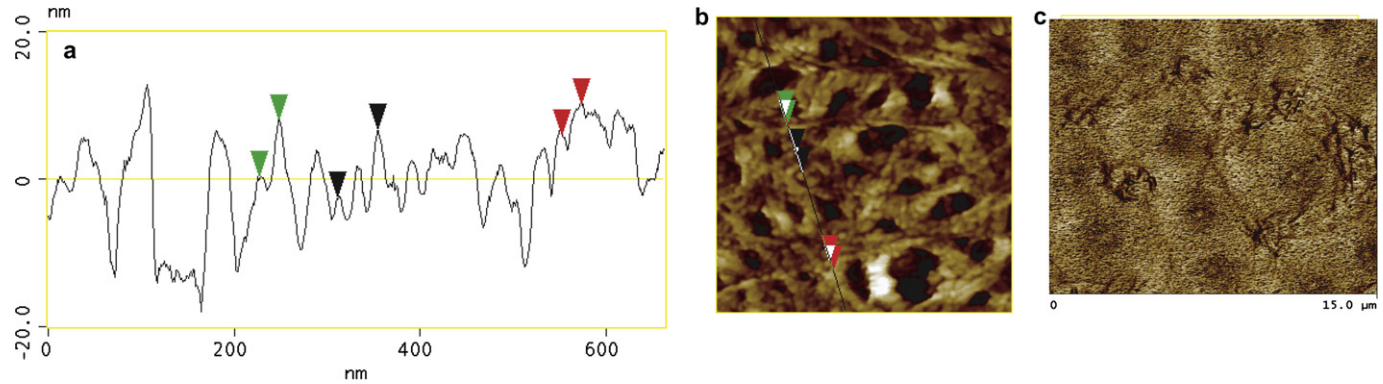

Fig. 9. (a) Height profile of the imprint surface of *H. rufescens* demineralized in EDTA and fixed. (b) A phase image of the area corresponding to (a). The height profile was made along the indicated line. (c) Phase image of a low resolution scan of the tissue used in (a and b). Note that the imprint centers appear to be less stiff than the surrounding areas. The softer areas of the imprint centers correspond to the center annuluses stained by colloidal iron as in Fig. 5a and b.

Dosidicus gigas. In general, however, the organization appears more regular as an ordered mesh as described above.

The phase image of Fig. 9c indicates that the imprint centers are doughnut shaped and are softer, *i.e.* less stiff, than the surrounding material. This region is the same size as that stained by colloidal iron as shown in Fig. 5a and b. This is consistent with the notion that the centers, that function as nucleation sites, were the resulting sites of "mineral bridges", that had the constitution of an organic/mineral mixture. When demineralized, such areas would naturally be softer than the more intact organic framework.

3.4. Chitin assays

Chitin assays were performed on demineralized framework material after demineralization in EDTA in unfixed conditions. The results are summarized in Table 1.

The results are consistent with the expectation that with digestion the weight fraction of chitin is measured to increase. As our digestion methods were not aggressive and were designed to remove only modest amounts of protein from the top layers, the modest increases in chitin weight fraction observed are expected. Moreover, the level of chitin is found to be higher than reported in other studies (*e.g.* Poulicek, 1983), but certainly consistent with the levels reported by Goffinet and Jeuniaux (1979) for other mollusks. Our assays are also consistent with the significant amounts of chitin observed *via* AFM and histochemical staining with WGA-FITC. Chitin assays can be prone to slight overestimates due to the fact that it is known that several proteins within the framework are glycosylated and that the glycosyl moieties of some of them may contain glucosamine residues. Given the consistencies as just noted, however, we believe such overestimates, if any, are quite modest.

4. Mechanical properties and modeling

4.1. An interlamellar layer constitutive model

The results and extractions of material properties from tensile data such as shown in Fig. 11 below can be analyzed using the model for layered nacre shown in Fig. 10. The model is based on a familiar assumption that load is transferred from the organic matrix to the ceramic tiles by interfacial shear, *i.e.* by "shear lag". Analysis of Fig. 10a and b yields an approximate expression (*e.g.* Gao, 2006; Gao et al., 2003) for the effective (elastic) shear modulus, G_p, of the interlamellar matrix

$$\frac{1}{E} = \frac{4g}{G_p(1-g)^2\rho^2} + \frac{1}{(1-g)E_c}. \quad (1)$$

In Eq. (1), G_p is the interlamellar shear modulus to be inferred from the tensile tests, assumed to be linear elastic as in an expression $\tau = G_p\gamma$ with τ and γ defined in Fig. 10c; E is the measured tensile modulus of nacre tested in the configuration of Fig. 10b; g is the volume fraction of interlamellar matrix; ρ is the aspect ratio (*i.e.* the ratio of diameter to thickness) of the ceramic tiles; and E_c is the modulus of the $CaCO_3$ tiles. To extract estimates for G_p from the analysis given in Fig. 10c, we note that f, the fraction of chitin in the interlamellar matrix, as estimated from our chitin assays is $f \sim 0.064 - 0.069$, with an average value of $\langle f\rangle = 0.066$. If we next assume that roughly one half the fibers are collinear with the direction of shear and one half are in the shear direction, then $\tilde{f} = 0.25$. Finally, we estimate the geometrical factor, $\sin^2 2\phi$ as $\langle \sin^2 2\phi\rangle|_0^{\pi/4} = 0.5$. From these assumptions and estimates we obtain

$$G_p \approx \frac{1}{32} f E_f. \quad (2)$$

If we take as an estimate for E_f, $E_f = 137$ GPa (*e.g.* Nishino et al., 1999), then $G_p \approx 0.3$ GPa. The above estimate contains several competing sources of approximation. For one, the contributing, and most likely viscoelastic, stiffness of the protein has been ignored. On the other hand, we have assumed a maximal effect of chitin in contributing to the stiffness. Nonetheless, the estimate is thought to be of the correct order of magnitude and most likely within a factor of two of the actual value.

Table 1
Results of chitin assays as per the protocol described in Section 2.9

Condition of tissue	wt%
Tissue in water	6.4
Digested with trypsin	6.9
Digested with trypsin + proteinase K	6.5

4.2. Mechanical properties

Quasi-static tensile tests were carried out on both *H. rufescens* and *N. pompilius*; results are shown in Fig. 11. We use Eq. (1) to extract G_p based on measured values of E. We take the volume fraction of interlamellar matrix to be $g = t/h$, where t is the matrix layer thickness and h the tile thickness. As it happens, $g \approx 0.06 - 0.066$ which is fortuitously close to f the fraction of chitin in the organic matrix.

For *H. rufescens* we find $E = 70 \pm 5$ GPa. If we assume $E_c = 100$GPa, and $g = 0.063$, we find $G_p = 0.41$GPa. The assumed modulus $E_c = 100$ GPa is based on values quoted for intact monolithic $CaCO_3$ (see for example Gao, 2006). However, as was noted in connection with Fig. 2a and b as examples, ceramic tiles are infiltrated with organic material that would tend to reduce their stiffness. Direct measurements of tile stiffness are as yet unavailable. If E_c is assumed to be less than 100GPa, the estimate for G_p will be somewhat larger. Nonetheless, the agreement between our estimate of $G_p = 0.41$ GPa and the model estimate of $G_p \approx 0.3$ GPa is encouraging. For *N. pompilius*, we find $E = 60 \pm 6$ GPa, and with $\rho = 15$ and $g = 0.063$, we obtain $G_p = 0.31$ GPa in quite good agreement with our model estimate.

More refined estimates of the elastic, or possibly visco-elastic, response of nacre tablets would take into account the intracrystalline matrix and the true nature of the tablets as coherent nanocrystalline aggregates, *e.g.* as noted in the Introduction with references to Rousseau et al. (2005) and Oaki and Imai (2005). It is easy to see, as noted in the Introduction, that this would lead to reductions in tablet stiffness of at least 10% which would place our estimates of overall nacre stiffness, that use our model estimate of interlamellar stiffness, in even better accord with experiments as shown in Fig. 11. In addition, future analysis will need to consider the mechanical response of the interlamellar layer as it will be affected by degrees of hydration and protein content (*e.g.* Feng et al., 2000). Quite dramatic effects of water and protein content on stiffness the component areas of the beaks of the squid *D. gigas* have recently been reported by Miserez et al. (2008). The variations they report span a full factor of 10 in elastic modulus and thus similar possible variations need be explored for the biopolymer framework of nacre shell.

5. Discussion

5.1. Macromolecular mapping

A summary of the results just presented is shown in Fig. 12. Here we map at least five distinct zones characterized by populations of macromolecular constituents. Chitin is indeed present

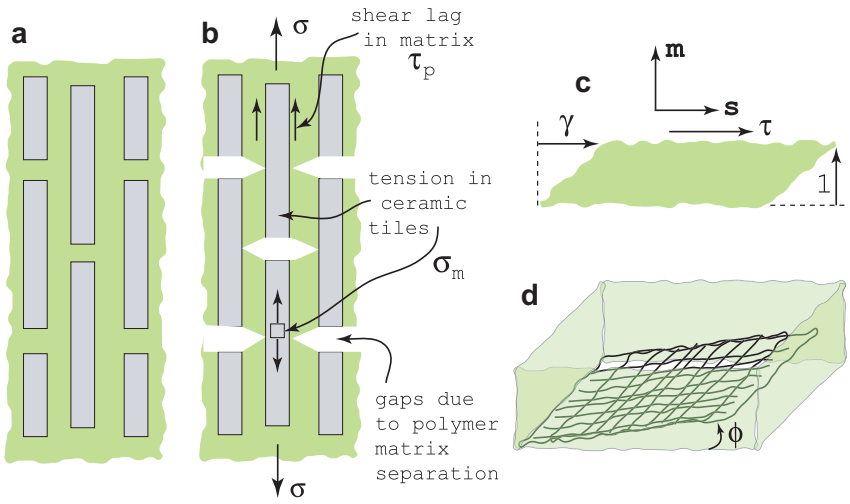

Fig. 10. (a) Shear lag model for the tensile stiffness of layered nacre. Tiles are illustrated as gray rectangles and the intertabular and interlamellar matrices in green. Note that the area fraction of organic matrix is exaggerated for illustration. (b) Same as (a) but now illustrating the separation of tiles from matrix at the tile ends and the "shear lag" process. (c) An illustration of simple shear of the interlamellar layer; this assumes the imposition of deformation gradient $\mathbf{F} = \mathbf{I} + \gamma\mathbf{sm}$. Chitin fibers are assumed to lie along directions inclined by angle ϕ to the interlamellar plane as illustrated in (d) of the figure. This leads an estimated stretch of chitin fibers $\lambda^2 \approx 1 + \gamma \sin 2\phi$ and a normal strain in such fibers of $e_n \approx 1/2\gamma \sin 2\phi$. The elastic energy stored within such fibers is then $\mathscr{E} = 1/2E_f\gamma^2 \sin^2 2\phi$, where E_f is the tensile modulus of chitin. Finally we assume that the volume fraction of such fibers contributing to resistance is $f_e = \bar{f}f$, where f is the total volume fraction of chitin and $\bar{f}$ the fraction of chitin fibers oriented to contribute to resistance in the direction of the applied shear stress. The model is completed by setting the elastic energy density stored in the fibers to that of a linear elastic solid with shear modulus G, *i.e.* set $\bar{f}f/8E_f\gamma^2 \sin^2 2\phi = 1/2\, G\gamma^2$ to obtain $G = 1/4\bar{f}fE_f \sin^2 2\phi$.

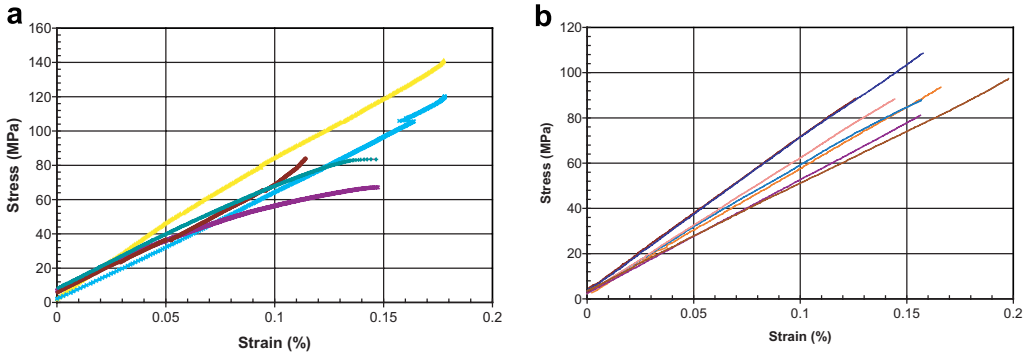

Fig. 11. (a) Quasi-static uni-axial tensile stress *vs.* strain response, at a nominal strain rate of 10^{-4} s^{-1}, at 20 °C for nacre specimens of *H. rufescens*. (b) Same as (a) but for *N. pompilius* nacre. Tests conducted in-plane, *i.e.* parallel to the interlamellar nacre layers as *per* Fig. 10b.

and forms a structural core that underlies the interlamellar framework and is a major, if not the major, constituent of the intertabular matrix. At the center of an interlamellar layer is a region rich in carboxylates and aragonite nucleating proteins (Fig. 4 and 6); there are, however, instances where two or more such localized regions are identified by our labeling (*e.g.* Figs. 2b and 6b). Surrounding the center is an annulus rich in acidic sulfates as seen in Fig. 5a and b.

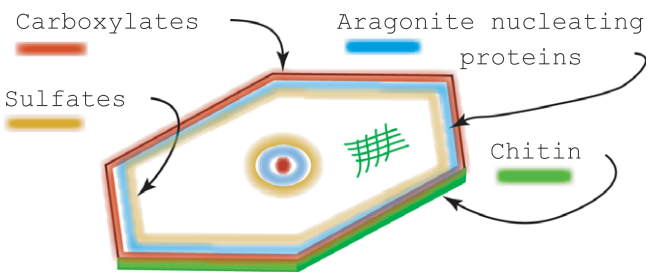

Fig. 12. Macromolecular "map" of the surface of an interlamellar layer; molecular types are indicated as found *via* the labeling methods described above. The intertabular matrix, and its molecular constituency, is also indicated.

Chitin is identified underlying the interlamellar layers (Fig. 3b and c) and is found to be present in high concentration in the intertabular matrix (Fig. 2c and d). The intertabular matrix is also rich in carboxylates and sulfates consistent with the findings of Nudelman et al. (2006) for *N. pompilius* and *A. rigida*. As far as the organization of chitin, the observations are not conclusive. The AFM images indicate that the fibers are often arranged in bundles (Fig. 8c) and span lengths of at least 1 μm (Fig. 8a and b). It is likely they form a mesh that forms the structural core of the interlamellar framework and eventually becomes a major constituency of the intertabular matrix. Based on limited data obtained from X-ray and electron diffraction on several mollusks (excluding *H. rufescens*), Weiner and Traub (1980) and Weiner et al. (1983) identified chitin in the β form within the organic matrix. In mollusks such as *N. repertus*, chitin was reported to be well ordered. In others, such as *M. californianus*, chitin was not observed by their methods. No chemical assays for chitin were reported in those studies. In contrast we find very high chitin contents in *H. rufescens* with a probable mesh-like organization. This was the basis of our model analysis of the interlamellar shear stiffness of Section 4.1 that provided an estimate consistent with experiment.

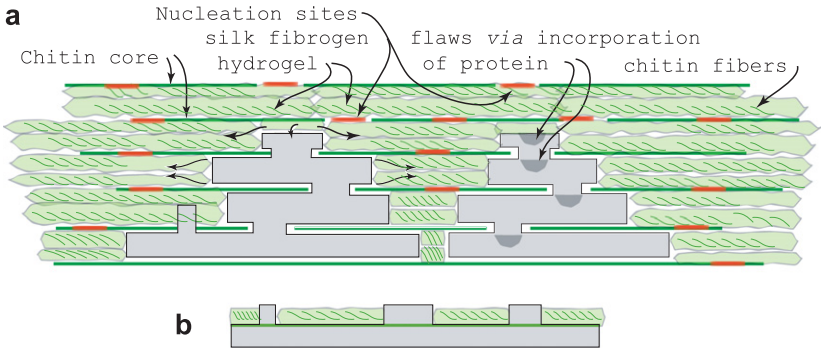

Fig. 13. (a) Model paradigm for the growth process of nacre in *H. rufescens* as described in the text. (b) Illustration of multiple mineral bridge formation leading to nano-(poly)crystalline tablets on individual layers.

5.2. Implications for nacre nucleation and growth

Fig. 13 summarizes our findings of a possible growth mechanism for nacre in *H. rufescens*. We envision an organic template as described most recently by Addadi et al. (2006) and as described for gastropods by Cartwright and Checa (2006), built upon a structural chitin core. Chitin fibers, however, are seen to project into what becomes a silk hydrogel into which mineral nucleates and grows. The chitin core is likely organized in a patch-like structure and possibly crystalline over some length scale, again as summarized most recently by Cartwright and Checa (2006). Our tapping mode AFM images reveal this fibrous core and provide direct evidence for its organized nature (*e.g.* Fig. 8c). Of the growth paradigms proposed over the years, we suggest that the data supports a scenario whereby tiles grow through the interlamellar layers thereby forming "stacks" that are readily reproduced as "flat pearls" as shown in Fig. 1c. As tiles grow laterally, *i.e.* within a layer, and water is displaced, both chitin and silk-like protein are accumulated within the intertabular matrix. This accounts for the chitin concentrating at the intertabular regions as labeled in Fig. 3a–c. Both chitin and protein are also accumulated within the interlamellar layers between the tiles and chitin core.

De novo nucleation is believed to occur at sites that result in the central regions labeled by aminoacridone, colloidal iron, and polyclonal antibodies labeling aragonite nucleating proteins. Here concentrations of negatively charged sulfates and carboxylates concentrate Ca^{++}. On the other hand, such sites on the surface of the interlamellar layers may also be preferential sites for the penetration of tiles growing in the c direction, or for the growth of a new tile atop one abutting an interlamellar layer. Such sites are indicated in red in Fig. 13a. Thus we do not describe the interlamellar layers as porous *per se*, but rather that they are built on a fibrous network (*i.e.* a core) with a protein hydrogel embedded in and sandwiching this core. Moreover, we expect there to be multiple nucleation sites on any given layer, possibly with a random distribution suggested by the observation of the occasional appearance of two or more new tiles on the top of growing stacks (*e.g.* Fig. 1c). Such multiple nucleation would lead to the nano- (poly)crystalline structure of individual tiles as described recently by Rousseau et al. (2005) who used AFM tapping mode scans to reveal nano-crystalline structure and by Oaki and Imai (2005). This scenario is sketched in Fig. 13b and we note that the process relies on a picture like ours for gastropods such as *H. rufescens* that have a mesh-like core that allows for the transmission of multiple mineral bridges per tablet as suggested, for example, by Cartwright and Checa (2006). Of course, our model also allows for the possibility of calcium carbonate precursors, such as the (chemically unstable) amorphous precursors discussed by Watabe et al. (1976) and Nassif et al. (2005), that are formed elsewhere and transported to the sites of tile growth. Such a possible scenario has also been discussed recently by Addadi et al. (2006) and mentioned by Cartwright and Checa (2006).

As tiles grow through the layers to form a new tile on the higher layer, the "mineral bridges" that are formed absorb the macromolecules that are part of the site. Organic material extends some distance into the thickness of the tile. This helps explain the more rapid dissolution of mineral at the tile centers during demineralization and the center structures seen in etched tiles or on demineralized layers (*e.g.* Fig. 2a and b). It also explains the origin of "flaws" that exist in all tiles that limit the fracture toughness. This too is illustrated in our model of Fig. 13a.

6. Summary and conclusions

We have advanced the understanding of the molecular structure of the organic framework of *H. rufescens* nacre. By combining histochemical optical microscopy, with AFM scanning probe microscopy and mechanical property analysis, we have provided a description of the organic framework that leads to a reasonable assessment of the mechanical response of the nacre composite and provides a specific picture for constructing a detailed model for nacre's nucleation and growth process. Our conclusions are, on the one hand, consistent in essential content with those of Nudelman et al. (2006) who studied *N. pompilius* and *A. rigida*, yet provide additional perspective on the structural makeup of the nacre organic framework. The distribution and role of chitin, in particular, has been revealed with much more clarity, with additional resolution of chitin's distribution within the framework. Important elements of detail remain to be elucidated.

A particular point of detail that remains to be clarified is the precise mechanism of propagation of a "stack" of tiles from one lamella to the next. Our results suggest that the nucleation sites identified at the tiles' centers may well be preferred sites for either tile penetration through interlamellar layers or be sites where preferred heterogeneous nucleation of new tiles occurs. This point of detail requires further clarification. Moreover, there is the interesting suggestion that precursors of calcium carbonate may be a kinetically favorable mechanism for transporting $CaCO_3$ to the sites of tile growth and most importantly nucleation (Watabe et al., 1976; Sikes et al., 2000; Nassif et al., 2005; Addadi et al., 2006). Advancing our understanding of the structural makeup of the framework is, of course, vital for eventually sorting this out.

As for mechanical properties, we suggest that these provide fresh and valuable insight for assessing molecular structural models of the framework. Two areas of research appear warranted here. First, the documentation of dynamic properties, as opposed to simple static response, will be of great value since the organic framework is most likely visco-elastic and the dynamic response that

results from that is intimately linked to molecular structure (*e.g.* Doi and Edwards, 1986). Methods of microrheology (*e.g.* Crocker et al., 2000) should be applied to framework tissue in various states of hydration to determine such properties. Of course, simple dynamic (*e.g.* cyclic deformation) property measurements are of value and are much more readily performed. Curiously, no such data exists to our knowledge. Finally, we suggest that the effects of both water content and gradients in protein content be studied as these have been shown to be of quite significant importance in mediating mechanical response in biological chitin/protein frameworks, *e.g.* Miserez et al. (2008).

Acknowledgments

The authors thank Dr. Rafael Sentandreu and Dr. Luis Castillo of the Universitat de Valencia for their help in performing the chitin assays that have been so valuable for our analysis. We are also grateful to Dr. Steve Weiner and his colleagues at the Weizmann Institute of Science, Rehovot, Israel for supplying us with polyclonal antibodies as noted in the text.

References

Addadi, L., Weiner, S., 1985. Interactions between acidic proteins and crystals: stereochemical requirements in biomineralization. Proc. Natl. Acad. Sci. USA 82, 4110–4114.

Addadi, L., Weiner, S., 2001. Biomineralization-crystals, asymmetry and life. Nature 411, 753–755.

Addadi, L., Weiner, S., Geva, M., 2001. On how proteins interact with crystals and their effect on crystal formation. Z. Kardiol. 90, 92–98.

Addadi, L., Joester, D., Nudelman, F., Weiner, S., 2006. Mollusk shell formation: a sourse of new concepts for understanding biomineralization processes. Chem. Eur. J. 12, 980–987.

Aizenberg, J., Black, A.J., Whitesides, G.M., 1999. Control of nucleation by patterned self-assembled monlayers: fabrication of ordered arrays of oriented, uniform calcite crystals. Nature 397, 4500–4509.

Baeuerlein, E., 2000. Biomineralization: From Biology to Biotechnology and Medical Application. Wiley-Vch, New York.

Belcher, A.M., Wu, X.H., Christensen, R.J., Hansma, P.K., Stucky, G.D., Morse, D.E., 1996. Control of crystal phase switching and orientation by soluble mollusc-shell proteins. Nature 381, 56–58.

Belcher, A.M., Gooch, E.E., 2000. Protein components and inorganic structure in shell nacre. In: Biomineralization. Wiley-Vch, New York, pp. 221–249.

Bevelander, G., Nakahara, H., 1969. An electron microscope study of the formation of the nacreous layer in the shell of certain bivalve mollusks. Calcif. Tissue Res. 3, 84–92.

Cariolou, M.A., Morse, D.E., 1988. Purification and characterization of calcium-binding conchiolin shell peptides from the mollusk, *Haliotis rufescens*, as a function of development. J. Comp. Physiol. B 157, 717–729.

Cartwright, J.H.E., Checa, A.G., 2006. The dynamics of nacre self-assembly. J. R. Soc. Interface 4, 491–504.

Checa, A.G., Rodriguez-Navarro, A.B., 2005. Self-organization of nacre in the shells of *Pterioida* (Bivalvia: Mollusca). Biomaterials 26, 1071–1079.

Crenshaw, M.A., 1972. The soluble matrix of *Mercenaria mercenaria* shell. Biomineral Res. Rep. 6, 6–11.

Crenshaw, M.A., Ristedt, H., 1976. The histochemical localization of reactive groups in septal nacre from *Nautilus pompilius*. In: Omori, M., Watabe, N. (Eds.), The Mechanisms of Biomineralization in Animals and Plants. Tokai University Press, Toyko.

Crocker, J.C. et al., 2000. Two point microrheology of inhomogeneous soft materials. Phys. Rev. 85, 888–891.

Doi, M., Edwards, S.F., 1986. The Theory of Polymer Dynamics. Oxford Science Pub, Oxford.

Evans, A.G., Suo, Z., Wang, R.Z., Ahsay, I.A., He, M.Y., Hutchinson, J.W., 2001. Model for the robust mechanical behavior of nacre. J. Mater. Res. 16, 2475–2484.

Falini, G., Albeck, S., Weiner, S., Addadi, L., 1996. Control of aragonite or calcite polymorphism by mollusk shell macromolecules. Science 271, 67–69.

Feng, Q.I., Cui, F.Z., Pu, G., Wang, R.Z., Li, H.D., 2000. Crystal orientation, toughening mechanisms and a mimic of nacre. Mat. Sci. Engin. C 11, 19–25.

Gao, H., 2006. Application of fracture mechanics concepts to hierarchial biomechanics of bone and bone-like materials. Int. J. Fracture 138, 101–137.

Gao, h., Baohua, J., Jager, I.L., Arzt, E., Fratzl, P., 2003. Materials become insensitive to flaws at nanoscale: lessons from nature. PNAS 100, 5597–5600.

Geoghegan, W.D., Ackerman, G.A., 1997. Adsorption of horseradish peroxidase, ovomucoid and antiimmunoglobulin to colloidal gold for the indirect detection of concanavalin A, wheat germ agglutinin and goat antihuman immunoglubulin G on cell surfaces at the electron microscope level: a new method, theory, and application. J. Histochem. Cytochem. 11, 1187–1200.

Goffinet, G., Jeuniaux, C., 1979. Distribution et importance quantitative de la chitine dans les coquilles de mollusques. Cahiers Biol. Mar. 20, 341–349.

Gotliv, B.A., Addadi, L., Weiner, S., 2003. Mollusk shell acidic proteins: in search of individual functions. Chembiochem 4, 522–529.

Gregoire, C., 1957. Topography of the organic components in mother-of-pearl. J. Biophys. Biochem. Cytol. 3, 797–808.

Gregoire, C., 1972. Structure of the molluscan shell. In: Florkin, M., Scheer, B.T. (Eds.), Chemical Zoology. Academic Press, New York, pp. 45–102.

El Gueddari, N.E., Rauchhaus, U., Moerschbacher, B.M., Deising, H.B., 2002. Developmentally regulated conversion of surface-exposed chitin to chitosan in cell walls of plant pathogenic fungi. New Phytologist 156 (1), 103–112.

Harrington, B.J., Hageage, G.J., 2003. Calcoflour white: a review of its uses and applications in clinical mycology and parasitology. Lab. Med. 34, 361–367.

Hayat, M.A., 1993. Staining and Cytochemical Methods. Springer, Berlin.

Herth, W., 1980. Calcofluor white and congo red inhibit microfibril assembly of poteriochromonas: evidence for a gap between polymerization and microfibril formation. J. Cell Biol. 87, 442–450.

King, T.P., Brydon, L., Gooday, G.W., Chappell, L.H., 1987. Silver enhancement of lectin-gold and enzyme-gold cytochemical labelling of eggs of the nematode Onchocerca gibsoni. Histochem. J. 19, 281–287.

Levi-Kalisman, Y., Addadi, L., Weiner, S., 2001. Structure of the nacreous organic matrix of a bivalve mollusk shell examined in the hydrated state using cryo-TEM. J. Struct. Biol. 135, 8–17.

Lowenstam, H.A., Weiner, S., 1989. On Biomineralization. Oxford University Press, New York.

Lukes, J., Volf, P., Lom, J., 1993. Detection of chitin in spores of Myxobolus muelleri and M. subepithelialis (Myxosporea Myxozoa). Parisitol. Res. 79, 439–440.

Maeda, H., Ishida, N., 1967. Specificity of binding hexapyranosyl polysaccharides with fluorescent brightener. J. Biochem. 62, 276–278.

Mann, S., Webb, J., Williams, R.J.P., 1989. Biomineralization: Chemical and Biological Perspectives. VCH, Cambridge.

Manne, S., Zaremba, C.M., Giles, R., Huggins, L., Walters, D.A., Belcher, A., Morse, D.E., Stucky, G.D., Didymus, J.M., Mann, S., Hansma, P.K., 1994. Atomic force microscopy of the nacreous layer in mollusk shells. Proc. R. Soc. Lond. B 256, 17–23.

Marin, F., Pokroy, B., Luquet, G., Layrolle, P., De Groot, K., 2007. Protein mapping of calcium carbonate biominerals by immunogold. Biomaterials 28, 2368–2377.

Miserez, A., Schneberk, T., Sun, C., Zok, F.W., Waite, J.H., 2008. The transition from stiff to compliant materials in squid beaks. Science 319, 1816–1819.

Mutvei, H., 1979. On the internal structure of the nacreous tablets in molluscan shells. Scanning Elect. Microsc. 2, 457–462.

Mutvei, H., 1977. The nacreous layer in *Mytilus*, *Nucula*, and *Unio* (Bivalva): crystalline composition and nucleation of nacreous tablets, Calcif. Tissue Res. 24, 11–18.

Nassif, N., Pinna, N., Gehrke, N., Antonietti, M., Jager, C., Colfen, H., 2005. Amorphous layer around aragonite platelets in nacre. PNAS 102 (36), 12653–12655.

Nishino, T., Matsui, R., Nakamae, K., 1999. Elastic modulus of the crystalline regions of chitin and chitosan. J. Polymer Sci. B: Polymer Phys. 37 (11), 1191–1196.

Nudelman, F., Gotliv, B.A., Addadi, L., Weiner, S., 2006. Mollusk shell formation: mapping the distribution of organic matrix components underlying a single aragonite tablet in nacre. J. Struct. Biol. 153, 176–187.

Oaki, Y., Imai, H., 2005. The hierarchical architecture of nacre and its mimetic material. Angew. Chem. Int. Ed. 44, 6571–6575.

Pearse, A.G.E., 1968. Histochemistry. Theoretical and Applied I. Little, Brown and Co., Boston.

Peters, W., Latka, I., 1986. Electron microscopic localization of chitin using colloidal gold labeled with wheat germ agglutinin. Histochemistry 84, 155–160.

Poulicek, M., 1983. Chitin in gastropod operculi. Biochem. Syst. Ecol. 11, 47–54.

Ramaswamy, S., Dworkin, M., Downard, J., 1997. Identification and characterization of *Myxococcus xanthus* mutants deficient in calcofluor white binding. J. Bacteriol. 179, 2863–2871.

Rousseau, M., Lopez, E., Stempflé, P., Brendlé, M., Franke, L., Guette, A., Naslain, R., Bourrat, X., 2005. Multiscale structure of sheet nacre. Biomaterials 26, 6254–6262.

Ruiz-Herrera, J., 1992. Fungal Cell wall: Structure, Synthesis, and Assembly. CRC Press, Boca Raton.

San-Blas, G., Calderone, A., 2004. Pathogenic Fungi: Structural Biology and Taxonomy. Caister Academic Press, Norfolk, UK.

Sarikaya, M., Liu, J., Aksay, I.A., 1992. Nacre of abalone Shell: a Multifunctional Nanolaminated Ceramic-polymer composite material. In: Case, S. (Ed.), Results and Problems in Cell Differentiation in Biopolymers. Springer Verlag, Amsterdam, pp. 1–25.

Sarikaya, M., Liu, J., Aksay, I.A., 1995. Nacre: Properties, crystallography, morphology, and formation. In: Sarikaya, M., Aksay, I.A. (Eds.), Biomimetics: Design and Processing of Materials. American Institute of Physics, Woodbury, New York, pp. 35–90.

Schaffer, T.E., Inoescu-Zanetti, C., Proksch, R., Fritz, M., Walters, D.A., Almqvist, N., Zaremba, C.M., Belcher, A.M., Smith, B.L., Stucky, G.D., Morse, D.E., Hansma, P.K., 1997. Does abalone nacre form by heteroepitaxial nucleation or by growth through mineral bridges? Chem. Mat. 9, 1731–1740.

Sikes, C.S., Wheeler, A.P., Wierzbicki, A., Mount, A.S., Dillaman, R.M., 2000. Nucleation and growth of calcite on native versus pyrolyzed oyster shell folia. Biol. Bull. 198, 50–66.

Simkiss, K., Wilbur, K., 1989. Biomineralization, Cell Biology and Mineral Deposition. Academic Press, San Diego.

Wada, K., 1961. Crystal growth of molluscan shells. Bull. Natl. Pearl Res. Lab. 7, 703–785.
Wada, K., 1968. Mechanism of growth of nacre in bivalvia. Bull. Natl. Pearl Res. Lab. 13, 1561–1596.
Wada, K., 1972. Nucleation and growth of aragonite crystals in the nacre of some bivalve mollusks. Biomineralization 6, 141–151.
Wada, K., 1980. Initiation of mineralization in bivalve mollusks. In: Omori, M., Watabe, N. (Eds.), The Mechanisms of Biomineralization in Animals and Plants. Tokai University Press, Toyko.
Watabe, N., Meenakshi, V.R., Blackwater, P.L., Kurtz, E.M., Dunkelberger, D.G., 1976. In: Watabe, N., Wilbur, K.M. (Eds.), Mechanisms of Biomineralization in the Invertebrates and Plants. University of South Carolina Press, pp. 283–308.
Weiner, S., 2007. Weizmann Institute of Science, Rehovot, Israel, private communication.
Weiner, S., Traub, W., 1980. X-ray diffraction study of the insoluble organic matrix of mollusk shells. FEBS Lett. 111, 311–316.
Weiner, S., Traub, W., 1984. Macromolecules in mollusk shells and their functions in biomineralization. Phil. Trans. R. Soc. London Ser. B 304, 421–438.
Weiner, S., Talmon, Y., Traub, W., 1983. Electron diffraction of molluscan shell organic matrices and their relationship to the mineral phase, Int. J. Biol. Macromol. 5, 325–328.
Wheeler, A.P., Rusenko, K.W., George, J.W., Sikes, C.S., 1987. Evaluation of calcium binding by molluscan shell organic matrix and its relevance to biomineralization. Comp. Biochem. Physiol. 87B, 953–960.
Wheeler, A.P., Sykes, C.S., 1984. Regulation of carbonate calcification by organic matrix. Am. Zool. 24, 933–944.
Williams, G., Jackson, D.S., 1956. Two organic fixatives for acid mucopolysaccharides. Stain Technol. 31, 189–191.
Wise, S., 1970. Microarchitecture and mode of formation of nacre (mother-of-pearl) in pelecypods, gastropods, and cephalopods. Eclogae Geol. 63, 775–797.
Zaremba, C.M., Belcher, A.M., Fritz, M., Li, Y., Mann, S., Hansma, P.K., Morse, D.E., Speck, J.S., Stucky, G.D., 1996. Critical transitions in the biomineralization of abalone shells and flat pearls. Chem. Mater. 8 (3), 679–690.
Zentz, F., Bédouet, L., Alameida, M.J., MIlet, C., Lopez, E., Giraud, M., 2001. Characterization and quantification of chitosan extracted from nacre of the abalone *Haliotis tuberculata* and the oyster*Pinctada maxima*. Mar. Biotechnol. 3, 36–44.